Go Extra Miles: An Additional Error Correction Procedure Aimed to Further Improve Phase Unwrapping Accuracy and Reduce Creep Model Uncertainty

Zhangfeng Ma[1], Jihong Liu[2], Xiaojie Liu[3], Jia Hu[1], Cheng Zhou[1], Yan Cui[1], Shuhong Qin[1], Teng Huang[1], Zhen Li[4]

[1]School of Earth Sciences and Engineering, Hohai University, Nanjing 211100, Jiangsu, P.R. China

[2]School of Geosciences and Info-Physics, Central South University, Changsha 410083, Hunan, P.R. China

[3] School of Geological Engineering and Geomatics, Chang'an University, Xi'an 710054, Shaanxi P.R. China

[4] College of Surveying and Geo-informatics, North China University of Water Resources and Electric Power, Zhengzhou 450046, P.R. China

Corresponding author: Zhangfeng Ma (jspcmazhangfeng@hhu.edu.cn)

Key Points:

- We present a new method for automatically correcting unwrapping errors for InSAR time series, which first supports for multi-looked data.
- Integer Linear Programming from Compressed Sensing framework is used to calculate integer number of phase unwrapping error cycles.
- We reduce the creep model uncertainty of the San Andreas Fault creep section using the proposed phase unwrapping error correction.

Abstract

Interferometric Synthetic Aperture Radar (InSAR) phase unwrapping error is a major limiting factor on the InSAR-derived tectonic deformation velocity. This is particularly the case when atmospheric turbulence, large deformation gradient and strong phase noise exist. To address limitations of existing phase unwrapping error correction methods which are not supported for multi-looked InSAR data, here we present a new algorithm that integrates decorrelation phase correction, triplet phase closure (TPC) test and integer linear programming (ILP) to overcome this limit. The rationale behind is that we mitigate the phase inconsistence using decorrelation correction and then detect the phase unwrapping error magnitude using TPC. Next we borrow the ILP from Compressed Sensing that converts the phase unwrapping error correction to a sparse signal recovery problem. We demonstrated the validity of our method by using synthetic data and 5-years Sentinel-1 real data covering the Central San Andreas Fault creep section, where exists obvious tectonic deformation, strong atmospheric disturbance and decorrelated scatterers, and the inverted long-term creep model constrained by InSAR velocity after correction shows a lower uncertainty than that constrained by the uncorrected one.

Plain Language Summary

Interferometric Synthetic Aperture Radar (InSAR) interferograms can provide us with very high precision crustal deformation velocity map. Phase unwrapping error, however, is still a major barrier to achieve such high precision. In the past few years, a series of unwrapping error correction methods dependent on triangle phase closure have been developed. But these methods are based on an assumption that triangle phase closure only includes unwrapping errors. In common large-scale InSAR processing workflows, in order to reduce the burden of data processing, we usually multi-looked interferograms. Recently decorrelation phase is found to exist in the triangle phase closure of the multi-looked interferograms and it would break the prior assumption. The existing methods cannot cope with this broken assumption. To overcome it, we propose an error correction method. This method does not need to change the existing InSAR workflows, but only serves as an additional step to correct the unwrapping errors of multi-looked interferograms. Experimental results over Central San Andreas Fault show that unwrapping error correction is significant for estimating the interseismic rate, and the proposed error correction can further reduce the creep model uncertainty. This is significant for large-scale InSAR processing to obtain the millimeter scale tectonic deformation velocity.

1 Introduction

Interferometric Synthetic Aperture Radar (InSAR) is a rising geodetic tool to monitor the Earth's surface deformation such as the interseismic creep (Biggs *et al.*, 2007; Hetland and Hager, 2006; Scott *et al.*, 2020; Stramondo *et al.*, 2016; Walters *et al.*, 2011; Wright *et al.*, 2001; W Xu *et al.*, 2018), postseismic deformation (ElGharbawi and Tamura, 2015; Feng *et al.*, 2015; Wang and Fialko, 2018) and land subsidence (Chaussard *et al.*, 2014; Cigna and Tapete, 2021; Shirzaei *et al.*, 2021). The in-orbit satellites such as Cosmo-Skymed with the repeat cycle of 4-16 days and ALOS-2 with a revisit period of 14 days can offer relatively high spatio-temporal resolution InSAR observations. Also, benefit from the electronically steering antenna under Terrain Observation of Progressive Scans (TOPS) mode (De Zan and Guarnieri, 2006), Sentinel-1 constellation expands the imaging coverage to 250km, so at the same time shortens the revisit period to 6 days. The provided dense spatio-temporal InSAR measurements increase the potential of multiscale accurate

tectonic process studies. However, phase unwrapping errors, frequently occurring in cases with steep deformation gradient, strong atmospheric turbulence and phase noise, are still a challenge for deriving highly accurate InSAR measurements, especially for long wavelength deformation along with the tectonic process.

Success in phase unwrapping seems impossible when no prior assumption supports. To illustrate, it is impossible to ambiguously recover the absolute or relative phases of two neighboring points, which are blurred by noise and wrapped into $[-\pi,\pi)$. A certain phase continuity assumption that the absolute phase difference of neighboring points is less than π makes this problem clear. The recovery process attempts to capture the wrapped phase difference and add back the deduced 2π cycles. However, the desired phase difference would not be satisfied everywhere due to the above mentioned three elements. To handle with this issue, points violating this assumption should be discriminated. Path-following methods such as branch-cut (Ghiglia and Pritt, 1998) label those points that wrapped phase difference in closed paths is nonzero as residues. The unwrapping process would not include these residues. Regarding to path-independent methods such as *L^p-Norm* (Costantini, 1998; Ghiglia and Romero, 1996; Shanker and Zebker, 2010; Yu *et al.*, 2017), the recovery process would search for a minimized weighted distance sum in *P*-Norm sense between wrapped and unwrapped phase difference. Impose higher weights to high SNR (signal-to-noise ratio) regions and nearly zero weight to residues thus mitigate the effect of residues on solutions. Towards further reducing the phase difference, temporal information is considered. For instance, Extended Minimum Cost Flow (EMCF) method (Pepe and Lanari, 2006) is used first to alleviate spatial phase difference larger than π, and then 2D phase unwrapping is performed interferogram by interferogram using compensated phase difference. Another line of thought (Hooper and Zebker, 2007) converts spatial branch-cut theory to 3D through linking phase residues to construct a 3D discontinuity plane, so extend the phase continuity assumption to 3D. Although more reliable results can be obtained when this assumption reaches a maximum satisfaction, this prior assumption cannot be regarded as an infaillible law due to the ever-present phase noise and steep variation (local deformation gradient and atmospheric turbulence) in real interferograms. Once the phase residues are mis-estimated, phase unwrapping errors may occur whatever unwrapping method we use.

Recent researches (Biggs *et al.*, 2007; Fattahi, 2015; Xu and Sandwell, 2020) demonstrated that these unwrapping errors due to violating the phase continuity assumption can be discriminated. Triplet phase closure (TPC) check is an effective measure of phase unwrapping errors. Assuming that multi-looking and filtering cause no variability of phase (Liu and Pan, 2020), TPC of interferograms would concentrate on zero if no phase unwrapping errors exist, whereas the integer cycles of non-zero TPC can be described as a linear relationship with residual phase ambiguities in interferograms. To reduce the phase unwrapping errors, two kinds of approaches based on TPC have been tried, using an iterative unwrapping fashion or an unwrapping-correction manner. For the first kind (Hussain *et al.*, 2016), TPC is used to reweight all pixels in interferograms. Those pixels with no TPC will be labeled as “error-free” and then will be applied high cost, so little phase change will happen to these pixels in the re-unwrapping. Re-unwrapping of all interferograms will be conducted for a certain times, and in each unwrapping the cost will be refreshed. This method has been proven to be able to well preserve the long wavelength interseismic deformation without the necessity to remove the estimated deformation from wrapped interferograms in advance. However, in term of machine memory or computational efficiency, it is not practical for most of portable platforms to iteratively unwrap a large account of interferograms. Instead, the second kind

of approaches provides a two-step unwrapping procedure which is easier to implement. In the first step, phase unwrapping is performed by methods such as SNAPHU(Chen and Zebker, 2001), Stanford Method for Persistent Scatterers (StaMPS) (Hooper *et al.*, 2004), 3D Finite Difference (Costantini *et al.*, 2012) or 2D sparse MCF(Costantini and Rosen, 1999). Next, phase unwrapping error correction pixel by pixel is performed, which only consumes a little random access memory (RAM). In phase unwrapping error correction, TPC of each pixel in redundant Small BASeline (SBAS) interferograms is first obtained to construct an observation matrix L. Then a linear equation can be formed in $BX = L$ where B represents the incidence matrix of the SBAS graph and X is the phase unwrapping error to be estimated. A Least Squares (LS) method is proposed to obtain the solution (Fattahi, 2015). However, for most of redundant SBAS graphs, triangle loop number is always smaller than the interferogram number. Therefore, B is a rank deficient matrix. Moreover, LS method tends to obtain a globally smooth solution which will result in a mis-estimation for final solutions. For example, LS may obtain a solution of 0.6 for a pixel free of unwrapping error. To solve this issue, a Linear Absolute Shrinkage and Selection Operator (LASSO) (Park and Casella, 2008; Xu and Sandwell, 2020) is proposed to stabilize the solution through adding an *L-1* Norm regularization to the objective function of LS. LASSO attempts to get more refined solutions by constructing a penalty function, which makes it compress some regression variables, that is, the sum of the absolute values of the X should be less than a fixed value. Therefore, it forms some coefficients in X to be zero or it means the obtained solutions are sparse. Its favored sparsity is consistent with the characteristics of unwrapping errors to be estimated that a considerable number of pixels have no unwrapping error. However, similar to LS, the solutions of LASSO also have the smoothing property because its objective function also contains *L-2* Norm, which violates the characteristic that the unwrapping error is an integer multiple of 2π. The solutions of LASSO require to be rounded to their nearest integers, which is risky for scenarios with strong noise. Moreover, time-consuming penalty selection and a parameterization process in LASSO are also itself limiting factors when a large number of pixels in the queue. Given that the prior assumption that multi-looked data would not break the zero phase closure due to multiple-scattering of non-random effect is hard to satisfy (Zheng *et al.*, 2021), the above mentioned state-of-the-art techniques actually only support for single-looked data. In low coherence regions with strongly variable soil moisture, decorrelation phase induced by multi-looking or filtering would pose a larger effect on triplet closure than unwrapping errors, therefore mislead the estimation of ambiguity cycles to be corrected. An unwrapping error correction method simultaneously supporting for multi-looked and single-looked data is urgently expected.

To cope with these issues, in this study we exploit and improve a recently proposed method (Ma *et al.*, 2021) known as ILP (integer linear programming) which only supports for single-looked data. We incorporate the decorrelation phase correction, the Density-Based Spatial Clustering of Applications with Noise (DBSCAN) (Ester *et al.*, 1996) and ILP to make the correction of multi-looked data tractable. The rationale behind it is we mitigate the triplet phase inconsistence through decorrelation phase correction. As a result, the criterion that TPC only contains phase unwrapping errors would be easier to be satisfied. Then we use DBSCAN based on temporal coherence to automatic select the stable reference in TPC calculation, therefore provide a reliable TPC for the following correction. Besides, *L-0* Norm is generally accepted as the best criterion for sparse signal recovery. In this context, we still borrow ILP from Compressed Sensing (CS) topic to convert a non-convex *L-0* Norm optimization problem in unwrapping error correction to a solvable *L-1* Norm linear programming problem. We validate our method using synthetic data and 5 years Sentinel-1 TOPS data covering the creep section of Central San Andreas Fault (CASF). Moreover,

we explore the left clues in (Khoshmanesh *et al.*, 2015) that phase unwrapping errors maybe an observation error source and possibly enlarge the creep model uncertainty. We confirm this hypothesis and demonstrate that our approach can help to reduce the uncertainty of the creep model.

2 Method

To better illustrate our proposed method, we first give its schematic diagram as shown in Fig.1. In the first step, we set all wrapped SBAS interferograms as input data, and we perform decorrelation phase correction to them. In the second step, we unwrap all interferograms using StaMPS 3D method. In the third step, we calculate the temporal coherence and down-sample it into regular grids. In the four step, we perform DBSCAN algorithm to temporal coherence map and automatic select the reference region. In the fifth step, we calculate the TPC and discriminate points with unclosed triangle loops. In the sixth step, we construct the linear equation and perform ILP to those discriminated points. Finally, we add back the obtained ambiguity to original unwrapped interferograms.

In the following subsections, we are trying to answer four questions in this workflow: 1) how to correct decorrelation phase? 2) why we calculate temporal coherence? 3) how to automatic select stable reference for TPC calculation? 4) how to correct phase unwrapping error using ILP? The answers to these four questions are theoretical foundations of our method.

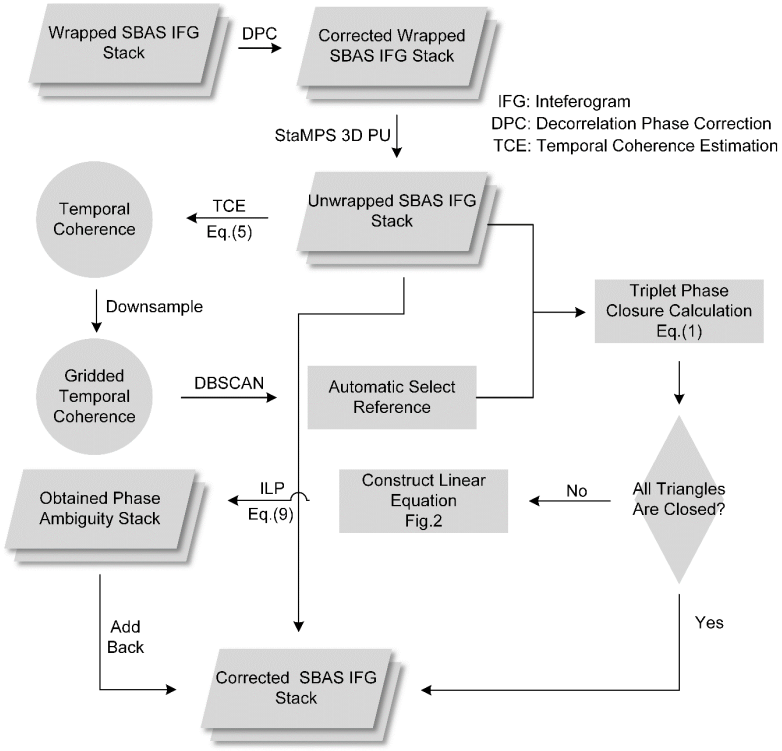

Figure 1. The schematic diagram of our proposed method.

2.1 Decorrelation Phase Correction

TPC $\Delta\phi^{TPC}$ of wrapped phase is formed by wrapped phase of three interferograms, which is defined as

$$\Delta\phi^{TPC} = \angle e^{j(\phi_{1,2}+\phi_{2,3}+\phi_{3,1})} \tag{1}$$

where $\phi_{i,j}$ means the wrapped phase and $\angle$ is taking phase of a complex number.

For single-looked data, $\Delta\phi^{TPC}$ will be strictly equal to zero. After multi-looking, $\Delta\phi^{TPC}$ would have a deviation from zero. After phase unwrapping, the lack of consistency will challenge distinguishing unwrapping errors from non-zero TPC. A singular value decomposition (SVD) method is introduced to mitigate the decorrelation phase (Michaelides *et al.*, 2019). This method defines the correction operation as a linear equation system:

$$\Delta\phi^{d}_{M\times1} = B^{\dagger}_{M\times K}\Delta\phi^{TPC}_{K\times1} . \tag{2}$$

where $B^{\dagger}$ is the pseudoinverse of the incidence matrix representing K triangle loops formed by M wrapped interferograms, and $\Delta\phi^{d}$ is the least-squares solution of decorrelation phase.

After solving $\Delta\phi^{d}$, the multi-looked or filtered interferograms need to remove it from the original phase.

For single-looked data, the solved $\Delta\phi^{d}$ is equal to zero because $\Delta\phi^{TPC}_{K\times1}$ of K triangle loops are all zero. Therefore, Eq. (2) is the principle base for simultaneously supporting for multi-looked and single-looked data.

2.2 The Relationship Between Temporal Coherence and Phase Unwrapping Errors

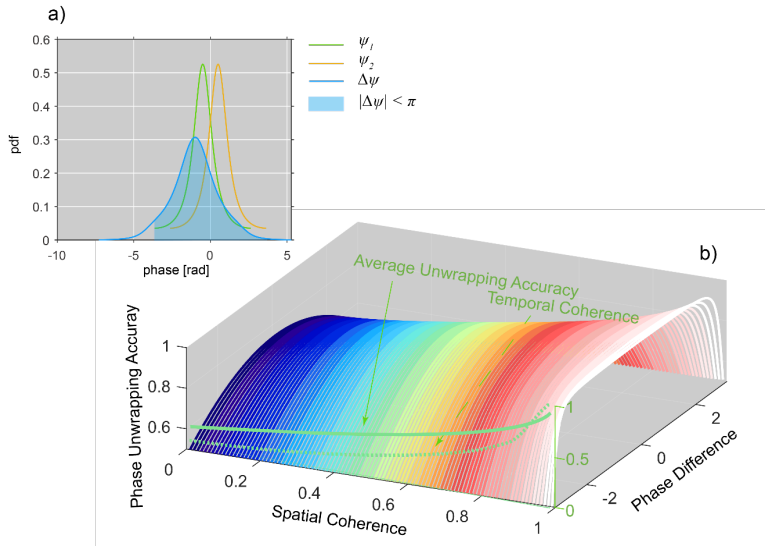

Figure 2. The relationship between temporal coherence and phase unwrapping error. (a) The probability density function of unwrapped phase and the convolved probability density function of phase difference. (b) The average unwrapping accuracy under different temporal coherence and spatial coherence

Given in (Jong-Sen *et al.*, 1994), the probability density function (*pdf*) for unwrapped phase can be described as

$$P_{\psi}(\psi|\gamma) = \frac{\Gamma(n+\frac{1}{2})(1-\gamma^2)^n\beta}{2\sqrt{\pi}\Gamma(n)(1-\beta^2)^{n+\frac{1}{2}}} + \frac{(1-\gamma^2)^n}{2\pi}F(n,1;\frac{1}{2};\beta^2) \tag{3}$$

where n is the number of looks, γ means the spatial coherence, β can be described as $\beta = \gamma\cos(\psi - \psi_T)$, ψ_T is the peak location of *pdf*, Γ denotes the gamma function and F represents the Gaussian hypergeometric function.

To obtain the *pdf* of phase difference between neighboring points ψ_1 and ψ_2, we can convolve two pdf. Its corresponding *pdf* is

$$P_{\Delta\psi}(\Delta\psi|[\gamma_1,\gamma_2]) = P_{\psi_1}(\psi_1|\gamma_1) \otimes P_{\psi_2}(\psi_2|\gamma_2). \quad (4)$$

Then we can directly obtain the desired probabilities of $|\Delta\psi| < \pi$ through integrating the convolved *pdf* in the interval of $(-\pi \quad \pi)$, which satisfy the phase continuity assumption (Itoh, 1982) and therefore can be theoretically regarded as the case with no unwrapping error. Fig.2a shows the *pdfs* of ψ_1=-0.5 and ψ_2= 0.5 both in $\gamma = 0.7$ and $n = 1$, also the convolved *pdf* of its related phase difference. The labeled transparent region means the circumstance with no phase unwrapping error. We compute the probability of unwrapping without error under different spatial coherence and phase difference situations. The results are presented as the phase unwrapping accuracy as shown in Fig.2b. We also calculated the temporal coherence ${}^{TP}\gamma$ of connected arc between ψ_1 and ψ_2. Its calculation can be formulated as

$${}^{TP}\gamma = \frac{1}{N}\left|\sum_{i=1}^{N} e^{j\cdot\{\psi_1 + f_N(\gamma_1) - \psi_2 - f_N(\gamma_2)\}}\right| \quad (5)$$

where $f_N(\cdot)$ is the phase noise simulation function and N means the simulated epoch number. In this simulation, we use $N = 20000$ aimed to make ${}^{TP}\gamma$ close to the true values. It should be noted that unwrapped phase can be formulated as the sum of phase modulo and ambiguities, thus temporal coherence in (5) computed by unwrapped phase difference is equivalent to that calculated by wrapped phase difference.

In Fig.2b, the temporal coherence simulated by different coherence situations is compared with the averaged unwrapping accuracy of different phase difference. It can be observed that there is a strong correlation between them. Considering that the wrapped phase difference cannot straightforward be treated as the unwrapping quality measure due to the existence of phase ambiguities, we use temporal coherence computed by wrapped phase difference as a reliable replacement.

2.3 DBSCAN for Automatic Selecting Reliable Reference in TPC Calculation

TPC is formed by unwrapped phase of three interferograms, which is formulated as

$$\Delta\psi^{TPC} = \psi_{1,2} + \psi_{2,3} + \psi_{3,1}. \quad (6)$$

Assuming that one pixel of these three interferograms contains no unwrapping error, $\Delta\psi^{TPC}$ will be equal to zero and requires no correction. This criterion is on a certain assumption that these three interferograms are unwrapped from a unique reference region of which phases are all regarded as zero. To this end, the phase of reference region should be subtracted from all interferograms after phase unwrapping, then TPC can be calculated. Nevertheless, if the selected reference contains unwrapping error, the calculation of TPC would fail because the error is transferred to the entire interferogram as a systematic bias. Therefore, the selection of reference region is significant for TPC calculation.

According to the description in Section 2.2, temporal coherence can measure the unwrapping accuracy, thus a region of high temporal coherence can potentially be a reliable reference region. However, the temporal coherence calculated by one arc cannot represent the phase quality of the connected point, so the average value of the 20 shortest arcs connected to a centered point is taken as the point temporal coherence. During the reference selection using temporal coherence, it is risky to simply search for the location of the highest point temporal coherence to determine the reference region. Imagine that the study region covers a large and another small region and both of them show good temporal coherence. Although the smaller one has a peak temporal coherence, it is surrounded by low coherence regions such as forests. These regions are likely to transfer the mis-estimated ambiguities to the isolated small region. If we choose the smaller region as a reference, it leads to the larger area needing to be corrected. Opposite, if we select a reference region in the large area, only a small area needs to be corrected. In summary, in addition to the high temporal coherence, dispersion degree of those regions should be considered simultaneously.

Therefore, we explore a method for automatic searching for a reliable reference. We apply Density-Based Spatial Clustering of Applications with Noise (DBSCAN) (Ester *et al.*, 1996) algorithm to seek the underlying temporal coherence pattern in an unsupervised way. The input data is in the three dimensions: temporal coherence, latitude and longitude. Prior to clustering, we down-sample scatters to a resolution of 500 m to reduce the computational burden of clustering (Fig.S1 is an example). We whiten the three column matrix to ensure their equal contributions to clustering. In DBSCAN, we set the neighborhood search radius to an empirical threshold of 0.2 and the minimum number of neighboring points for core point search to 200. Those points that cannot meet the above search criterion will be labeled as noise points. After DBSCAN, we select the cluster with the highest average temporal coherence and locate the region of peak temporal coherence in it as the final reference region. Then robust TPC can be calculated.

2.4 Phase Unwrapping Error Correction Using ILP

Compressed Sensing (CS) (Candes and Tao, 2005; Donoho, 2006), also known as Compressive Sensing, aims to recover sparse signals from few samples less than the Nyquist sampling theorem requires. Its scope coincides well with phase unwrapping error correction because of the sparsity of phase unwrapping errors (only partial errors differ from zero). In this section, we attempt to introduce how to correct phase unwrapping errors using ILP we borrow from the CS mathematical framework.

Let X represent the sparse phase ambiguity vector to be estimated and L denote TPC calculated from closed triangle loops from redundant SBAS interferograms. In matrix formulation, the closure phase is $L = BX$, where B is the incidence matrix designed from SBAS graph. The detailed construction process of B and L are given later in this section.

Given a prior assumption that X is a highly sparse vector (i.e., it has few unwrapping errors), then a reasonable optimization model is to search the sparest solution among those can produce L; that is,

$$\underset{X}{\operatorname{argmin}}\left(\left|X\right|_0\right) \quad \text{subject to} \quad BX = L \tag{7}$$

where $\left|X\right|_0$ means the number of non-zeros in X. The minimization of (7) is an NP-hard problem due to the nonconvexity of L0-Norm. To make this problem tractable, the basis pursuit approach in which $\left|X\right|_0$ is replaced with a continuous $\left|X\right|_1$ (Chen *et al.*, 2001):

$$\underset{X}{\operatorname{argmin}}\left(\left|X\right|_1\right) \quad \text{subject to} \quad BX = L \tag{8}$$

where $\left|X\right|_1$ is the sum of absolute values of X. We treated (8) as an equivalent linear programming problem. Given the desired integer feature of X, integer linear programming (ILP) is further applied to solve (8). Previous to search for an ILP solution, the mathematical formulation, in which all parameters to be estimated are non-negative, is required to be reformulated. We introduce two nonnegative slack vectors K to replace X, and (8) is transformed into (Donoho and Elad, 2003)

$$\begin{gathered}\underset{X}{\operatorname{argmin}}\left(f^T\left|K_p - K_n\right|_1\right) \text{ subject to } \begin{bmatrix}B & -B\end{bmatrix}\begin{bmatrix}K_p \\ K_n\end{bmatrix} = L \\ K_p, K_n \geq 0\end{gathered} \tag{9}$$

where f means the reciprocal of coherence vector, K_p means the positive slack vector and $-K_n$ is the negative slack vector.

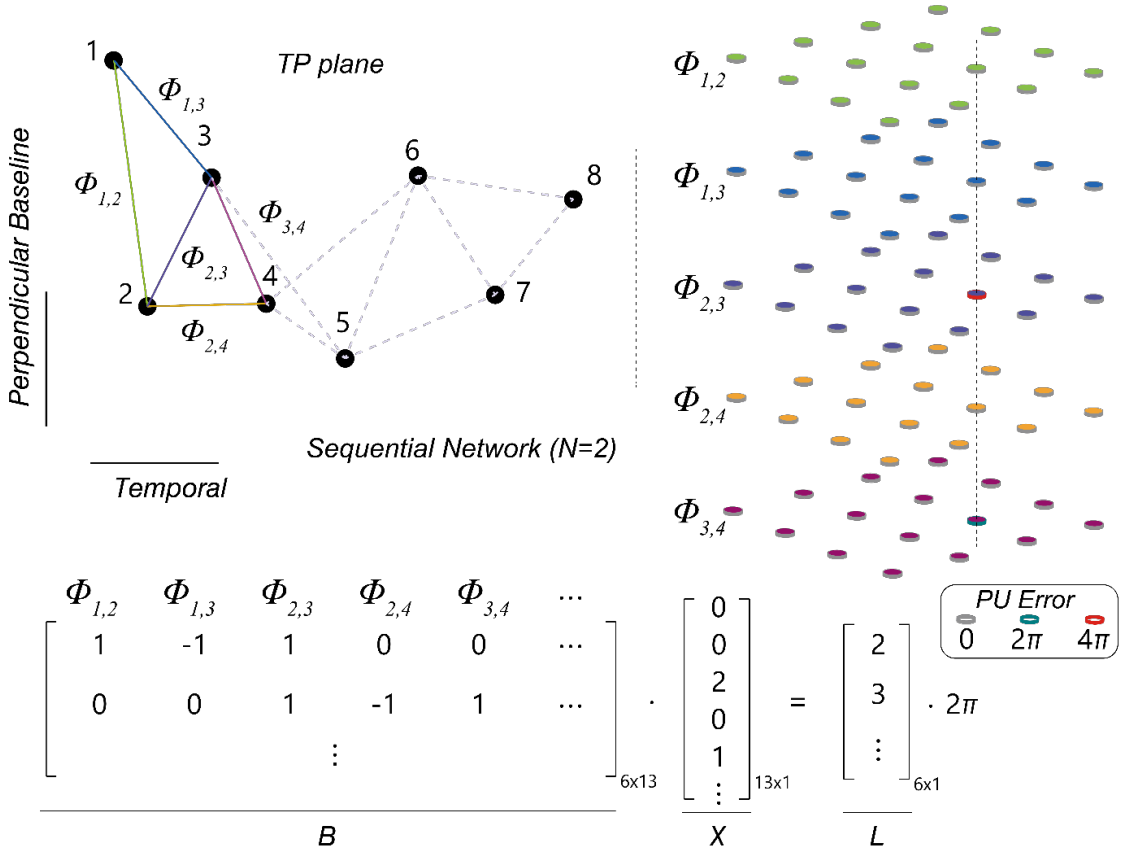

Figure 3. The schematic chart of triplet closure test and phase unwrapping correction process.

After solving (9), the integer ambiguities K is obtained by $K_p - K_n$. Although we can obtain the solutions through approximating (7) using (8), the left key problem is: under which condition the solutions to (7) and (8) are unique? A R.I.P criterion has been given (Donoho and Elad, 2003). For an incidence matrix B with a spark (the smallest rank of matrix) of m, the sparsity k of X ($k < m/2$) will not downgrade the success rate of CS recovery. Generally speaking, the less unwrapping errors and the more independent triangle loops in SBAS graph, unwrapping error is more likely to be corrected. If $k < m/2$ is fulfilled, unwrapping error would be completely corrected in theory. We discussed this in (Ma *et al.*, 2021) in details.

For completeness, here we give descriptions about the construction of B and L. In this paper, we use the sequential network proposed in (Fattahi *et al.*, 2016) as the SBAS graph. In Fig.3, triangle loops are constructed by neighboring epochs. Each triangle and interferogram denote the related row and column in B respectively, and the corresponding TPCs are presented in rows of L. For example, [1, -1, 1] in the first row of B means the closed triangle formed by interferograms $\psi_{1,2}$, $\psi_{1,3}$ and $\psi_{2,3}$. Its related TPC of 4π can be simply obtained. For the second triangle loop, in the same way, we can obtain [1, -1, 1] in the second row of B and the related TPC 6π.

3 Synthetic Data Test

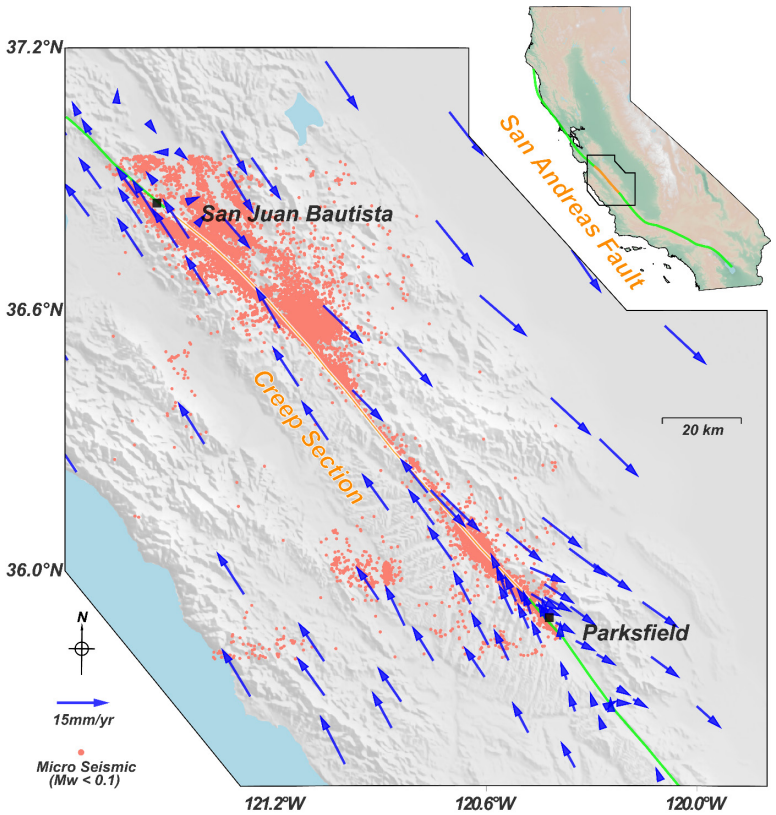

Figure 4. Map of the study region. The solid colored line represent the San Andreas Fault trace. The creep section is in orange and the other part is in green. The 2D velocity of Global Positioning System stations are shown in blue arrows. The salmon circles are recorded micro-seismicity (*Mw*

< 0.1). The hillshade shows the topographic relief of the study region derived from the Shuttle Radar Topography Mission (SRTM) 3-arc seconds data, which is also applied to the subfigure.

To test the ability of the method to correct the unwrapping errors, we randomly simulated a time-dependent creep model of ~140km creep section on the Central San Andreas Fault (CASF) (Fig.4) using fault geometry in (M. Khoshmanesh and M. Shirzaei, 2018; Khoshmanesh *et al.*, 2015). This creep section bounded by San Juan Bautista to the northwest and Parkfield to the southeast, is characterized as a nearly continuous right-lateral aseismic slip, with a rate of up to 34.5 mm/yr (Ryder and Bürgmann, 2008).

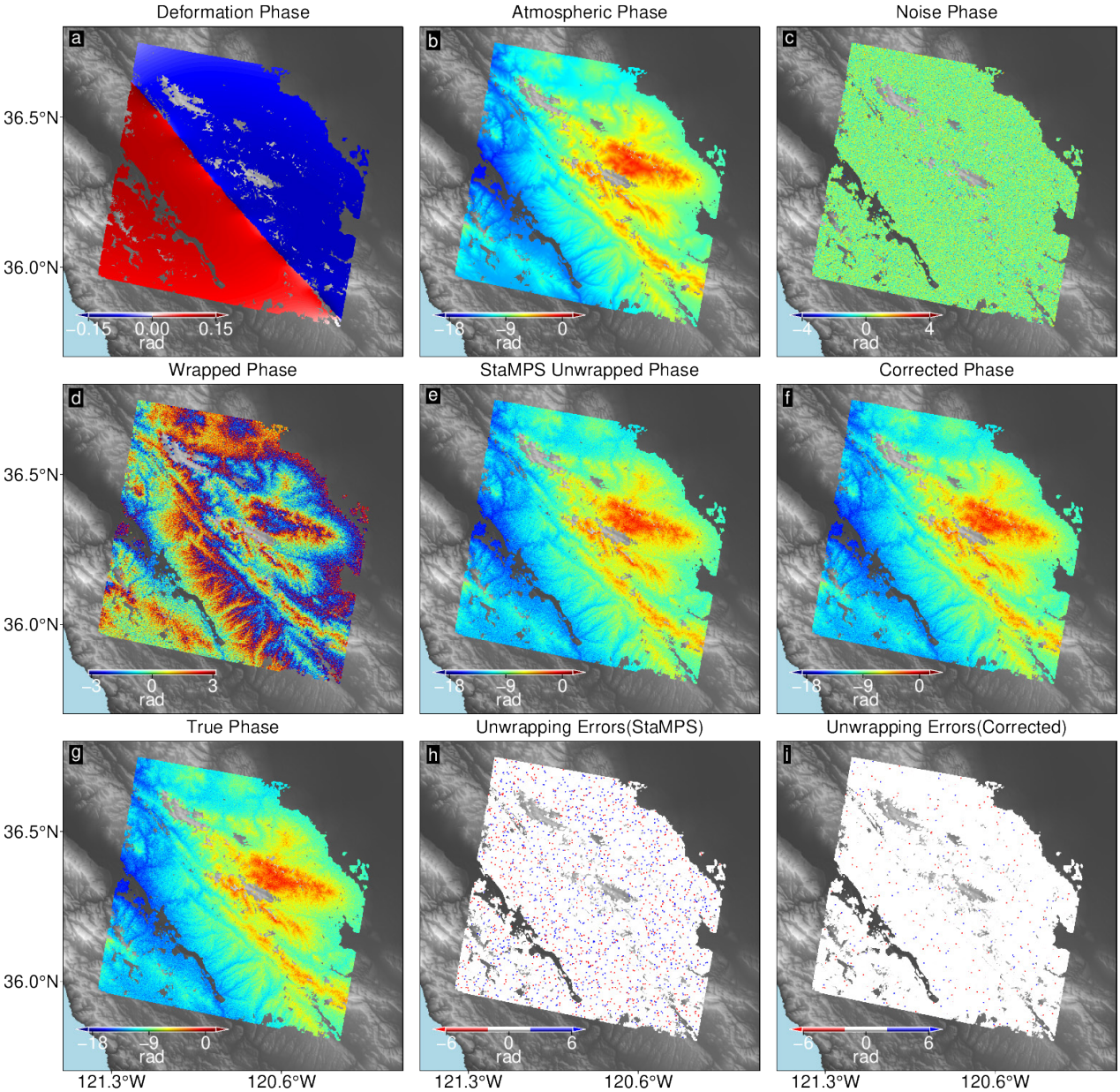

Figure 5. Unwrapped interferograms and unwrapping errors before and after correction. (a-c) are simulated interferogram components. (a) deformation phase. (b) atmospheric phase. (c) noise phase. (d) is the simulated interferogram and (e-f) are respectively unwrapping interferograms

before and after correction. (g) is the true phase values. (h-i) are respectively unwrapping errors before and after correction.

We set the simulated model as a two-layer fault (Fig.S2) composed of shallow and deep segments with different creep rates. Similar to checkboard test, shallow patches between 0km and 15km are imposed with a creep rate of 34.5mm/yr or 20mm/yr, and the shallow patches between 15km and 25km are set to a creep rate gradient (increase from 20mm/yr to 34.5mm/yr). To consider the effect of deep dislocation zone, we simulate this infinitely creeping zone ranging from 25km to 3000km with a long-term rate of 34.5mm/yr (Rolandone *et al.*, 2008). Both deep and shallow dislocations are set to be pure right-lateral strike slip.

We simulate 157 SAR images in SAR coordinate reference for each image with a constant heading angle of 190 and an incidence angle of 35. We generate the time-dependent deformation phase using simulated dislocations (Fig.5a). Additionally, noise phase are randomly simulated for each acquisition (Hanssen, 2001). Noise magnitude is corresponded with γ=0.6 (Fig.5c). We also simulate atmospheric phase delay for each time epoch using the atmospheric delay provided by Generic Atmospheric Correction Online Service (GACOS) (Yu *et al.*, 2018) (Fig.5b). Then we generate 465 small baseline interferograms using the simulated 157 single reference epochs. We multi-looked all simulated interferograms by a factor of 20 and 5 in range and azimuth direction respectively. We selected 1192214 sparse points referred to the true positions in the below real data test. We use StaMPS software to unwrap all interferograms with a 3-D method. Then we detect the phase unwrapping errors and correct them using the proposed method. Fig.5d and Fig.5e respectively show the selected wrapped interferogram and its unwrapped phase after StaMPS unwrapping. Fig.5f presents the corrected interferogram after correction by the proposed method. Compared to the true phase values (Fig.5g), their respective unwrapping errors are presented in Fig.5h-i. One can see that unwrapping errors before correction (Fig.5h) are distributed like salt-and-pepper whereas the unwrapping errors after correction (Fig.5i) of interferograms are greatly reduced.

Furthermore, we give a statistic of unwrapping error cycle numbers (2π as one cycle) for each point before and after error correction. Results are respectively shown in Fig.6a and Fig.6b. Compared to results without correction, the number of interferogram with unwrapping errors has an obvious decrease after correction. It can be seen from the histograms (Fig.6c) of two results that the error histogram before correction is around 3 and it is mostly near 0 after correction. We perform LOS velocity inversion using least squares method. The inverted LOS velocity of uncorrected results and corrected results are respectively shown in Fig.6e and Fig.6f. Their estimation error differing from true velocity (Fig.6d) are shown in Fig.6g and Fig.6h. It can be seen that the place of obvious velocity mis-estimation is consistent with that of the unwrapping errors. After PU correction, the overall velocity estimation error is reduced, it can be vividly seen from the histograms (Fig.6i) of velocity estimation before and after correcting the errors.

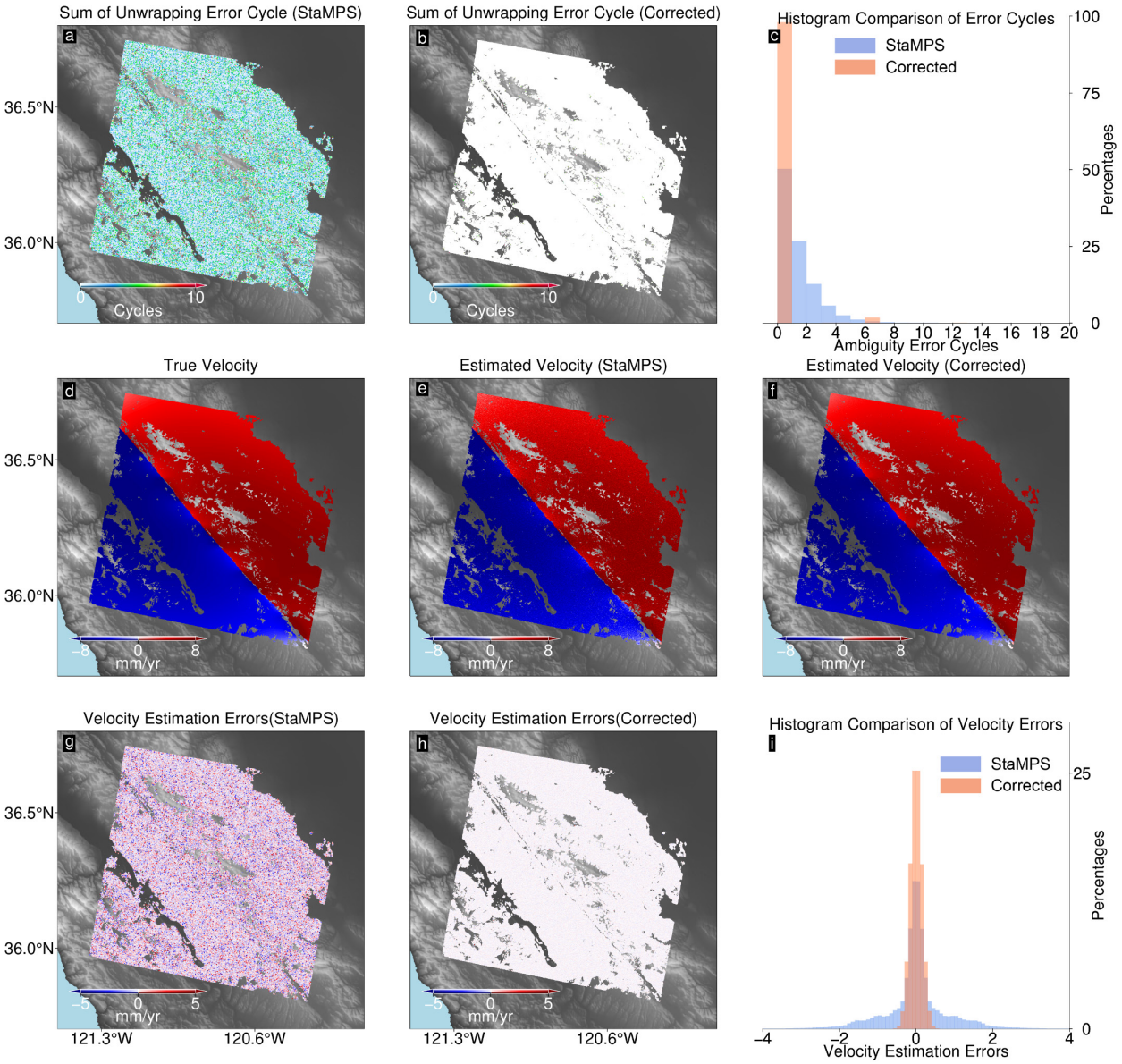

Figure 6. The number of unwrapping error cycles before and after correction, the inverted LOS velocity using corrected and uncorrected results, and respective velocity estimation error between true values. (a-b) The sum of unwrapping error cycles before and after correction. (c) Histograms of the number of error cycles before and after correction. (d) The true LOS velocity. (e) The inverted LOS velocity using results without correction. (f) The inverted LOS velocity using results with correction. (g-h) The estimation error of (e-f). (i) Histograms of (g-h).

Based on the estimated velocity before and after correction, we conduct a statistical test to reveal whether the unwrapping error will affect the creep model uncertainty which is a left clue in (Khoshmanesh *et al.*, 2015). We name this test as 80% percentile jackknife. In each jackknife, we randomly select 80% of samples and down-sample the selected samples to 500m resolution. In the creep model inversion, we generate the green function based on the pure right lateral dislocations and the effect of the deep dislocation is subtracted from down-sampled observations. We set the creep restricted between 0mm and 40mm which are the lower and upper boundary of slip respectively. We also perform a second order Laplacian operator to constrain the model

smoothness. Moreover, we automatically select the optimal model smooth factor through searching for the position of maximum curvature in L-curve (Hansen, 1994), which represents a trade-off between the slip smoothness and realistic of creep. For each creep inversion, a recursive constrained linear least squares method is used to approach the final solutions. The random sampling and inversion process are repeated 100 times. Mean creep rate constrained by two difference velocity are respectively shown in Fig.7b and Fig.7c. Through visual inspection, the two results only slightly differ in magnitude and they are very similar to the shape of the simulated creep (Fig.7a). Nevertheless, the absolute rate error standard deviation (STD) of two creep rate model has a significance difference. The absolute creep rate errors of the model constrained by results without correction (Fig.7d) are larger than that of results constrained by the corrected one (Fig.7e). Similarly, the STD of creep model constrained by the velocity without correction (Fig.7f) are larger than the creep model constrained by the velocity with correction (Fig.7g). The inverted LOS velocity residuals also show the outperformance of the corrected results (Fig.7h-i). It validates the hypothesis of (Khoshmanesh *et al.*, 2015) that PU errors can be a large misfit to creep model and have a negative effect on model uncertainty.

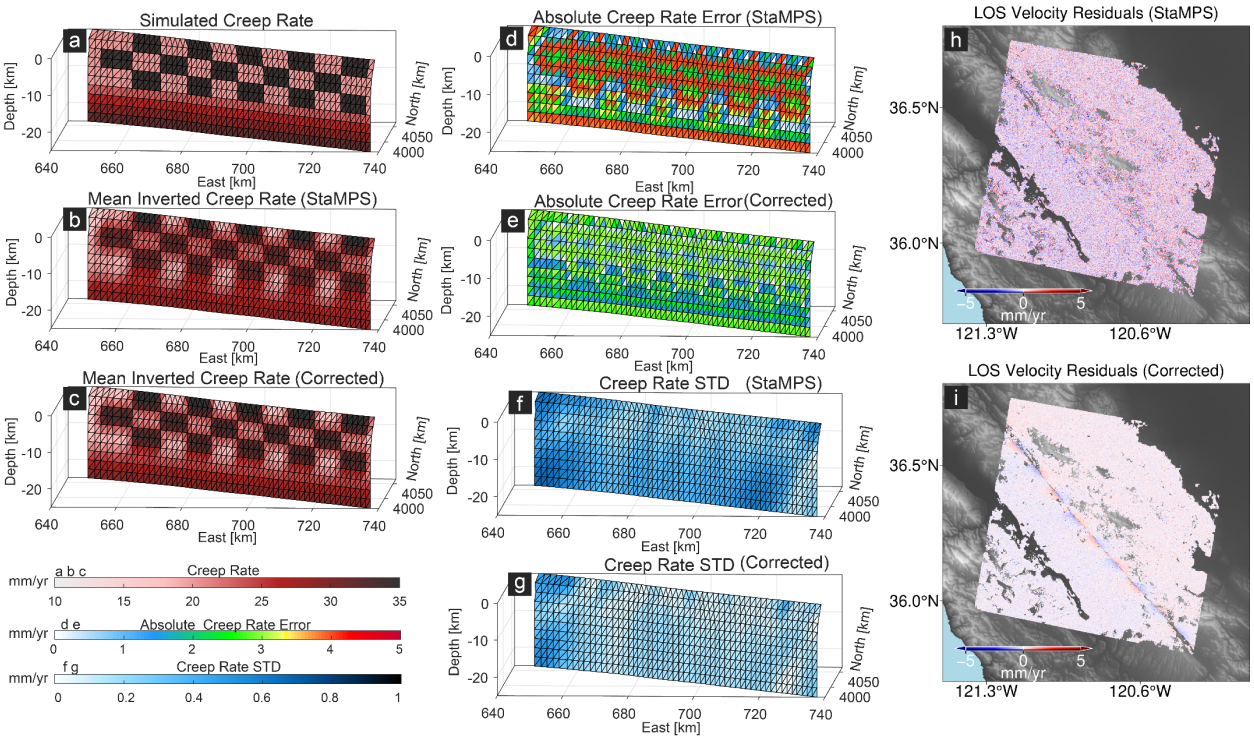

Figure 7. The inverted creep rate model and their model uncertainty in UTM reference. (a) The simulated creep rate. (b) and (c) are respectively the inverted mean creep rate constrained by jackknife results without correction and with correction. (d) and (e) are respectively absolute creep rate errors of mean creep rate inverted by results without correction and with correction. (d) and (e) are respectively model STD of jackknife results without correction and with correction. (h) and (i) are respectively LOS velocity residuals of forwarded LOS velocity of the mean creep rate for (b) and (c).

4 Real Data Test

We processed 157 SAR images acquired by Sentinel-1 in a descending track 157 between Mar 2015 and Aug 2020. We accomplished the co-registration task of 157 images through a two-step strategy. Geometrical co-registration method using external SRTM 30 DEM and 5cm 3D 1-sigma precise orbit is first performed to resample all images to a common reference, then followed by the Efficient Enhanced Spectral Diversity (EESD) (Ma *et al.*, 2020) technique to correct the residual azimuth mis-registration. Using this dataset, we generated 465 high-quality small baseline interferograms (the same SBAS graph in synthetic data test). Flat-earth correction and topographical phase removal were performed using SRTM and precise orbit. We multi-looked all interferograms by a factor of 20 and 5 in range and azimuth direction respectively, resulting a ~65m×65m ground pixel resolution. After multi-looking, we performed a decorrelation phase correction (Michaelides *et al.*, 2019) to mitigate the phase inconsistence (Zan *et al.*, 2015), therefore avoiding its effect on the non-zero triplet phase closure. The mitigation to the decorrelation phase is significant for phase ambiguity correction and its necessity which is rarely discussed is further given in Section 5.1.

To select reliable pixels with high SNR, we calculated temporal phase coherence of each independent pixel involved with 50 neighboring pixels. We chose an empirical threshold of 0.75 to preserve elite pixels. After thresholding, 1192214 elite pixels are left. To recover the absolute ambiguity number of wrapped phase, we performed phase unwrapping using StaMPS 3D algorithm. Detailed PU parameters we used are given in TABLE S1. After StaMPS 3D, we select the reference using DBSCAN algorithm and calculate the TPC. Then we correct the unwrapping errors using the presented new method.

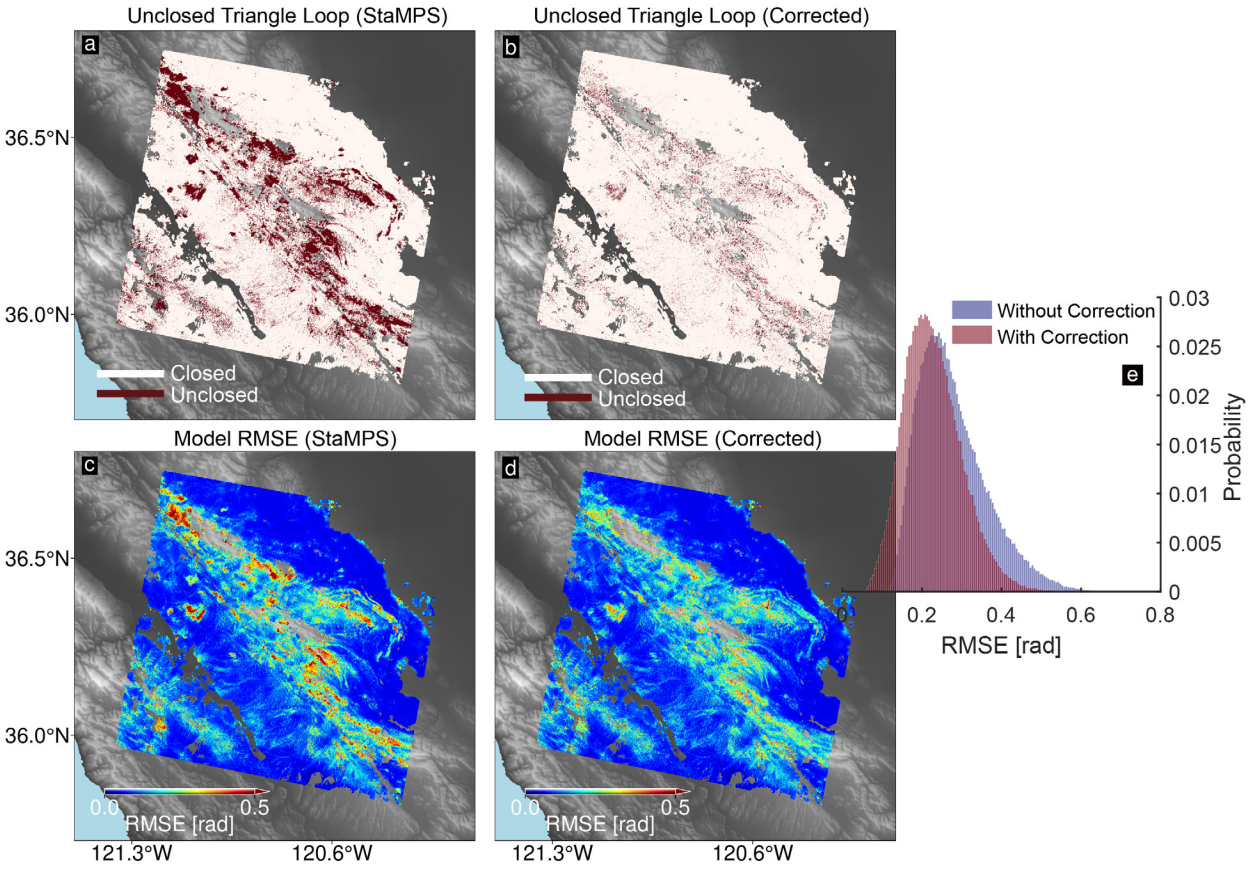

Figure 8. The points with unclosed triplet phase before and after correcting phase unwrapping errors and their corresponding root mean square error in single reference conversion. The points with unclosed phase are labeled as 1 (white color) and points without unclosed phase are labeled as 0 (red color). (a-b) Points with unclosed phase before and after correction. (c-d) Root mean square error of results before and after correction. (e) Histograms of (c-d).

In order to investigate whether the correction method is reducing phase unwrapping errors, we calculated the TPC of all interferograms before and after correction. We label points with nonzero phase closure as 1 and label points with zero phase closure as 0. Fig.8a and Fig.8b respectively show the calculated results. Compared to results before correction, points with unclosed triangle loops after correction decrease to a large extent. We also convert 465 SBAS interferograms to a common reference and calculate the corresponding root mean square error (RMSE) using least squares method. The distribution of RMSE before correction shows a strong correlation to those points with unclosed loops. Moreover, RMSE of those points without unclosed loops are close to 0. It can be seen from Fig.8c and Fig.8d that RMSE of results after correction shows a sharp decline. The histogram comparison in Fig.8e show an overall ~0.1 rad decrease for results after correction. The results validate the effectiveness of the proposed correction method.

Aimed to mitigate the influence of atmospheric phase delay on LOS velocity, we applied GACOS (Yu *et al.*, 2018) for all interferograms. The predicted atmospheric delay provided by GACOS matches the long-wavelength phase pattern in interferograms well (Fig.S3). After correction by GACOS, the average reduction in standard deviation is ~17% and therefore prove that the GACOS model can effectively screen the atmospheric phase of most of interferograms. We further estimated the displacement time series using a reweighted least squares method. In each iteration, weighted matrix is updated by the obtained residual from the previous estimation. The iteration process stopped once either the subsequent solution difference is less than 10^{-4} or the iteration number reaches 100. The LOS velocity is estimated by fitting a constant linear rate to final time series.

Subfigures in Fig.9a and Fig.9c respectively show the LOS velocity inverted by results without and with correction. The overlapped rectangles are GPS velocity projected in LOS direction. To focus on the performance of correction, we extract those points (Fig.9a and Fig.9c) with unclosed triangle loops in Fig.8a. We compare the velocity of those points to GPS velocity and calculate the related mean values and STD of velocity difference. We label them in white texts of top right corner of Fig.9a and Fig.9c. The mean difference and difference STD are respectively 1.8mm/yr and 4.1mm/yr for the results without correction. For the results with correction, the mean value of velocity difference decreases to 0.7mm/yr and STD reduces to 2.7mm/yr. The mean value and STD of results after correction have an improvement of ~61% and ~34%, respectively. It means velocity with correction are more accurate than that without correction. Furthermore, considering that interseismic creep is characterized as long wavelength deformation, we can calculate the STD of velocity in a small region in which velocity variation can be ignored, so for an accuracy comparison. The results in subfigures of Fig.9a and Fig.9c are down-sampled into sparse grids with a 500m resolution. For each grid, we calculate the related velocity STD. Scatter plot in Fig.9e shows the grid velocity STD comparison. Points lying under the diagonal line implies a higher velocity STD, therefore a relatively poor accuracy. Velocity STD of results without correction is obviously higher than that with correction. It demonstrates the high performance of our method.

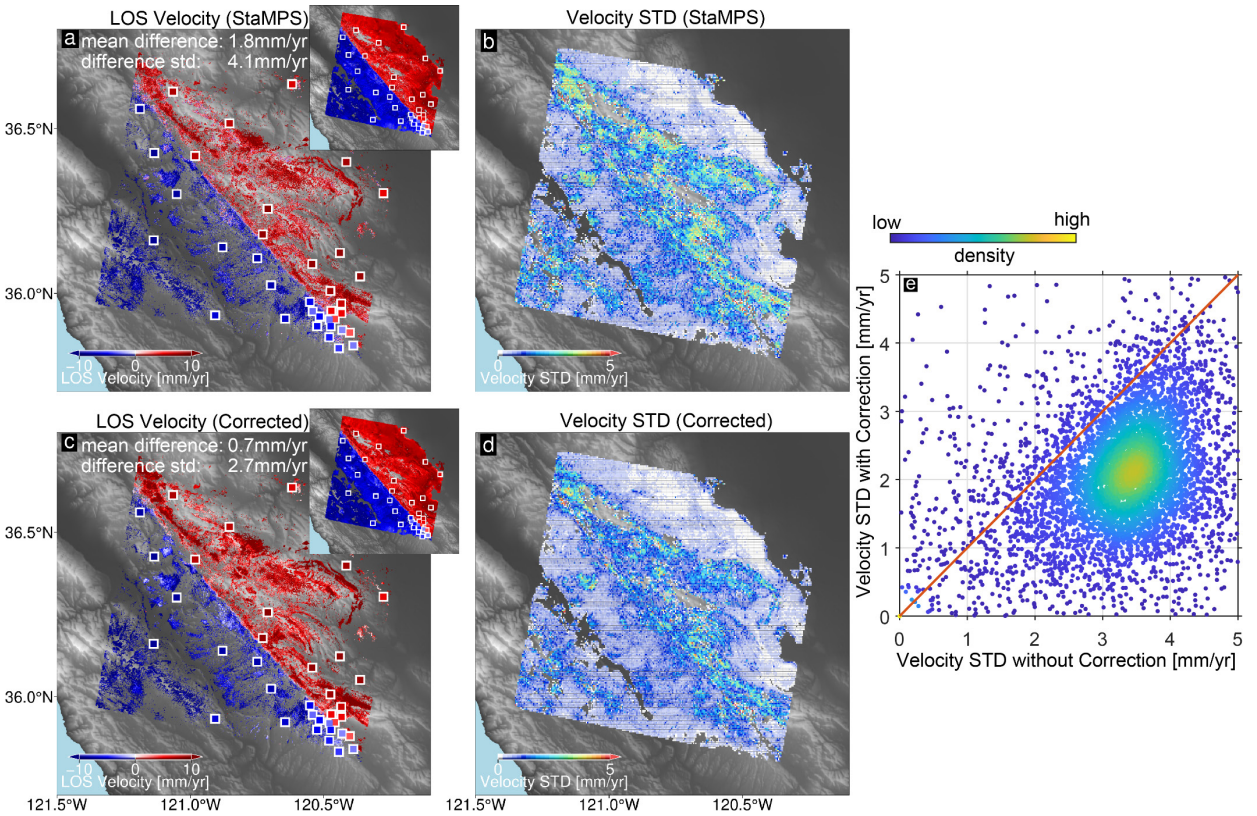

Figure 9. The estimated LOS velocity using results before and after correction, separately shown LOS velocity of points with unclosed phase in Fig.8a and their respective velocity STD. Subfigures in (a) and (c) are the estimated velocity using results without and with correction. The superimposed rectangles are GPS velocity in LOS direction. (a) and (c) also are velocity of those points with unclosed phase in Fig.8a and b. The white labeled texts in top right corner of (a) and (c) are mean values and STDs of velocity difference between InSAR and GPS. (b) and (d) are the estimated STD of gridded velocity in a resolution of 500 m rectangle. (e) Scatter plots are STD of LOS velocity respectively in (b) and (d).

Moreover, we also perform an 80% percentile jackknife test which is described in Section 3. We repeat the jackknife test 100 times and obtain the mean creep rate in Fig.10. Fig.10a and Fig.10c are respectively mean creep rate for results without correction and with correction. Similar to the synthetic data test, the inverted two creep models only slightly differ in magnitude. Nevertheless, the calculated STD of two creep rate model after correction has a significance difference. The creep rate STD in Fig.10b is much larger than the corrected results in Fig.10d. Thus it can be validated that unwrapping error correction is significant for reducing the creep model uncertainty.

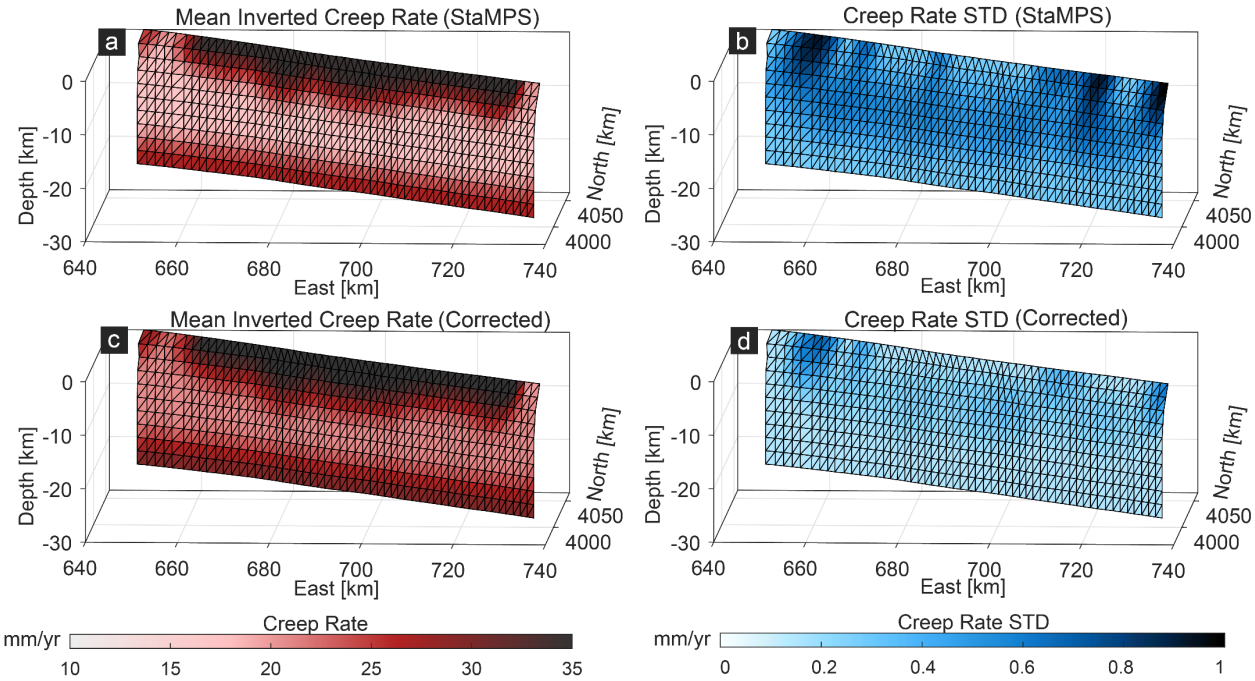

Figure 10. The inverted creep model and model uncertainty constrained by results without and with correction. (a) and (c) are respectively the inverted creep rate constrained by results without and with correction. (b) and (d) are creep rate STD of (a) and (c), respectively.

5 Discussions

5. 1 The Necessity of Correcting Decorrelation Phase for Fault Zones

To improve the phase SNR and further benefit phase unwrapping, a filtering or multi-looking is commonly performed directly after interferometric processing. For those multi-looked or filtered pixels, however, non-random effects of decorrelation potentially leads to non-zero closures. Moreover, for those low coherence regions with high variability of soil moisture (i.e. vegetation), decorrelation noise may pose a larger effect on triplet closure than unwrapping errors. When the decorrelation noise-induced closure surpasses π, it will lead to a mis-estimation of phase unwrapping error. In order to distinguish these non-zeros values from unwrapping errors, a decorrelation phase correction (Eq. (2)) is used in this paper. To discuss the necessity of correcting decorrelation phase, we give a result comparison to clarify it.

We unwrapped both the original and the decorrelation noise-corrected interferograms using the StaMPS 3D method. We calculated the ambiguity cycles of the unclosed triangle loop for two interferogram sets (Fig.11a-b). As can be seen, the ambiguity cycle decreases after performing decorrelation correction, especially in dense vegetation areas (Fig.11d) along the fault. We also present an unwrapping solution cost comparison for those two cases in Fig.11c. Phase unwrapping cost is the final convergence value of the objective function for each interferogram. A higher solution cost indicates a relatively high phase unwrapping burden and therefore a poor unwrapping performance (Chen and Zebker, 2001). Points lying under the diagonal line implies a higher solution cost, therefore a relatively poor performance.

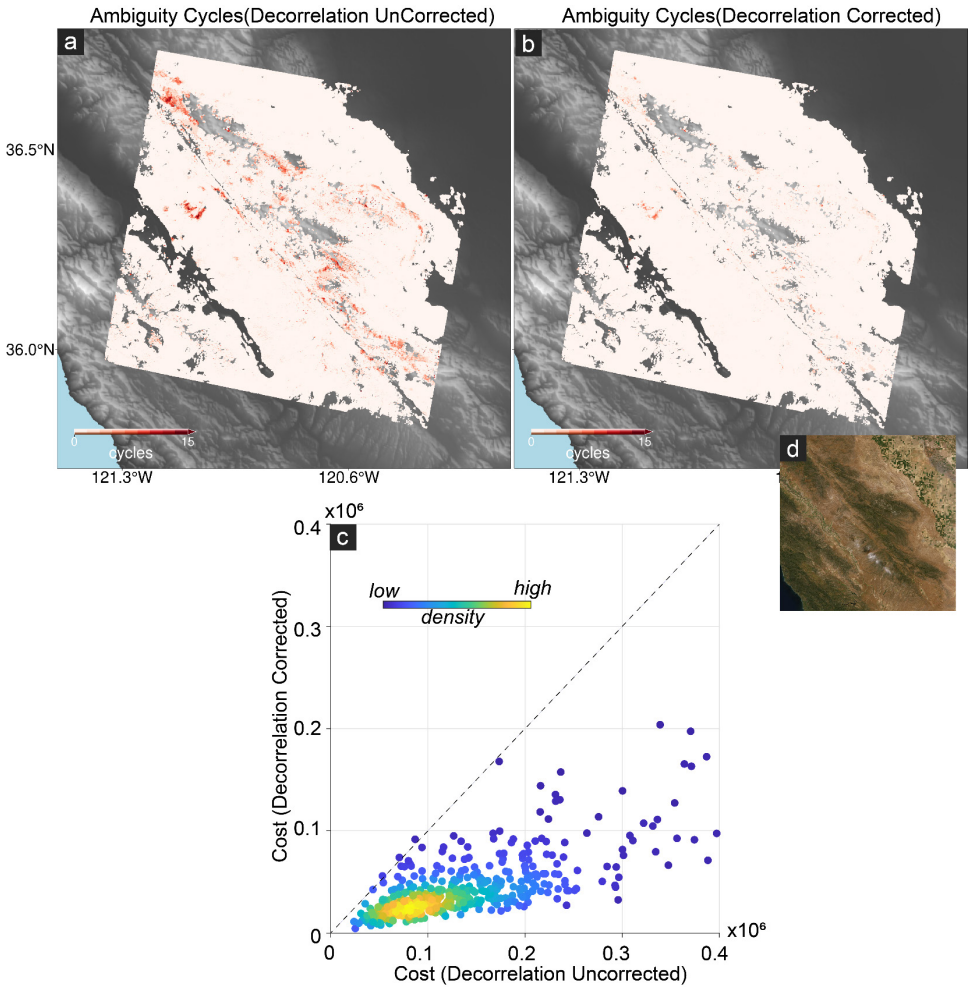

Figure 11. The calculated ambiguity cycles of unwrapping interferograms and the statistical solution cost. (a) and (b) are respectively the ambiguity cycle results without and with correction. (c) is the scatter plot of two unwrapping results. The scatter underlying the dashed line means the higher cost. (d) is an google-earth image corresponding to the drawing board of (a) and (b).

Although as shown above decorrelation phase correction can reduce phase unwrapping errors, its effect on ILP is still unknown. Here we performed a statistical experiment (Text S1) to further investigate the effect of phase unwrapping errors in varying degrees on the ILP solution. Two main results are respectively referred to as “Type I Error” and “Type II Error” (Fig.12), borrowed from the probability statistics. We defined “Type I Error” as that interferograms with unwrapping errors still contain unwrapping errors after ILP. “Type II Error” is defined as that unwrapping-error-free interferograms turn out to have unwrapping errors after ILP. When more phase unwrapping errors are input, probabilities of “Type I&II Errors” increase. More generally, the performance of ILP would drop along with the increase number of interferograms with unwrapping errors. Given that decorrelation phase removal is helpful to reduce unwrapping errors, a pre-decorrelation phase correction would also benefit the ILP solutions. From a compressed sensing point of view, the decrease of the number of interferograms with unwrapping errors represents the increase of the sparsity to be solved. The increase of sparsity indicates that the R.I.P criterion is easier to be satisfied when the number of independent triangle loops remains unchanged. Therefore, a pre-decorrelation correction is necessary.

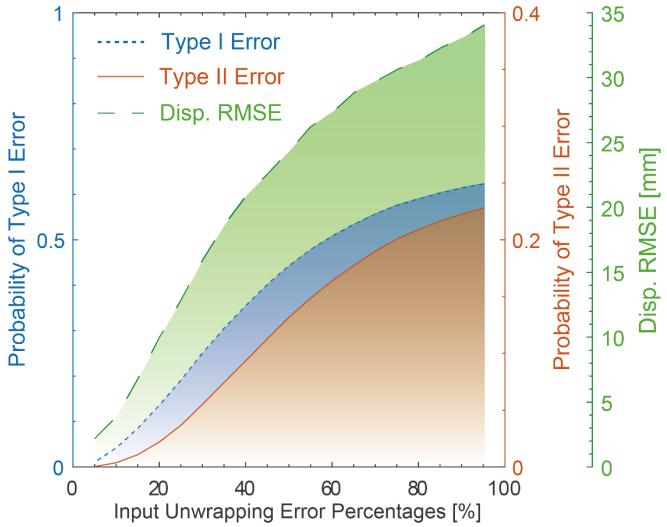

Figure 12. Statistical results of the performance of ILP when percentages of interferograms with unwrapping errors vary. The dotted blue line and the orange line respectively represent the probability of Type I and Type II Error. The dashed green line means the mean RMSE (root mean square error) of the inverted displacement time series.

5. 2 Coulomb Stress Change and Pore fluid Pressure Jointly Modulate the Creep Rate

Recent studies using space geodetic data reveal that interseismic creep can vary with a complex spatio-temporal feature (Mostafa Khoshmanesh and Manoochehr Shirzaei, 2018; X Xu *et al.*, 2018). In this study, we use the corrected 5-years InSAR time series to further study the dynamic characteristics of near-fault creep in CASF, and give an explanation for the potential mechanisms. It should be noted that InSAR time series we derived in this study still contain strong atmospheric noise though we already applied GACOS. Although we consider the residual atmospheric noise as temporally uncorrelated signals and therefore have little effect on the inverted LOS velocity, its effect on LOS time series cannot be ignored. An empirical approach integrating low-pass filtering in time and high-pass filtering in space has proven to be successful in mitigating the atmospheric noise in time series (Wang *et al.*, 2012). However, its prior assumption that the wavelength of atmospheric phase is longer than that of the signals of interest can result in the removal of a portion of interseismic deformation with long wavelength. Nevertheless, relative near-fault deformation time series can be regarded as robust for depicting the relative deformation history, since spatially correlated atmospheric noise can be eliminated in the time series difference of two neighboring pixels (Wang and Burgmann, 2020). We extracted the time series difference of eight points as described in Fig.13a. It can be seen from Fig.13d and Fig.13e that LOS time series has a noticeable change in late 2019. Given a triggering mechanism provided by (X Xu *et al.*, 2018) that static Coulomb stress change by nearby large earthquake modulates the fault creep rate, we derive two LOS rates respectively before and after Jul 2019 Ridgecrest Sequence, also the static Coulomb stress change induced by the sequence event.

We calculate the static Coulomb stress change at 1km depth using an elastic half-space model (Okada, 1992) with a Young's modulus of 80 GPa and a friction coefficient of 0.6. Coseismic slip (Fig.S5) model from (Feng *et al.*, 2020) is utilized to calculate the quasi-static stress change associated with the sequence event.

We suggest that the static Coulomb stress change modulate the creep rate, because it can explain the creep rate increase of point C-C' and D-D', also the almost invariable rate of point A-A' and B-B'. We detect the stress increase of 2.98 kPa and 2.82 kPa respectively for C-C' and D-D', and very small stress increase of 0.15kPa and 0.16 kPa respectively for A-A' and B-B'. From perspective of velocity-strengthening fault frictional properties (Perfettini and Avouac, 2004), a positive Coulomb stress change can cause an increase of creep rate for shallow faults, and a negative stress change can result in a creep rate drop. It coincidence well with the proposed conceptual model of creep triggering in (X Xu *et al.*, 2018).

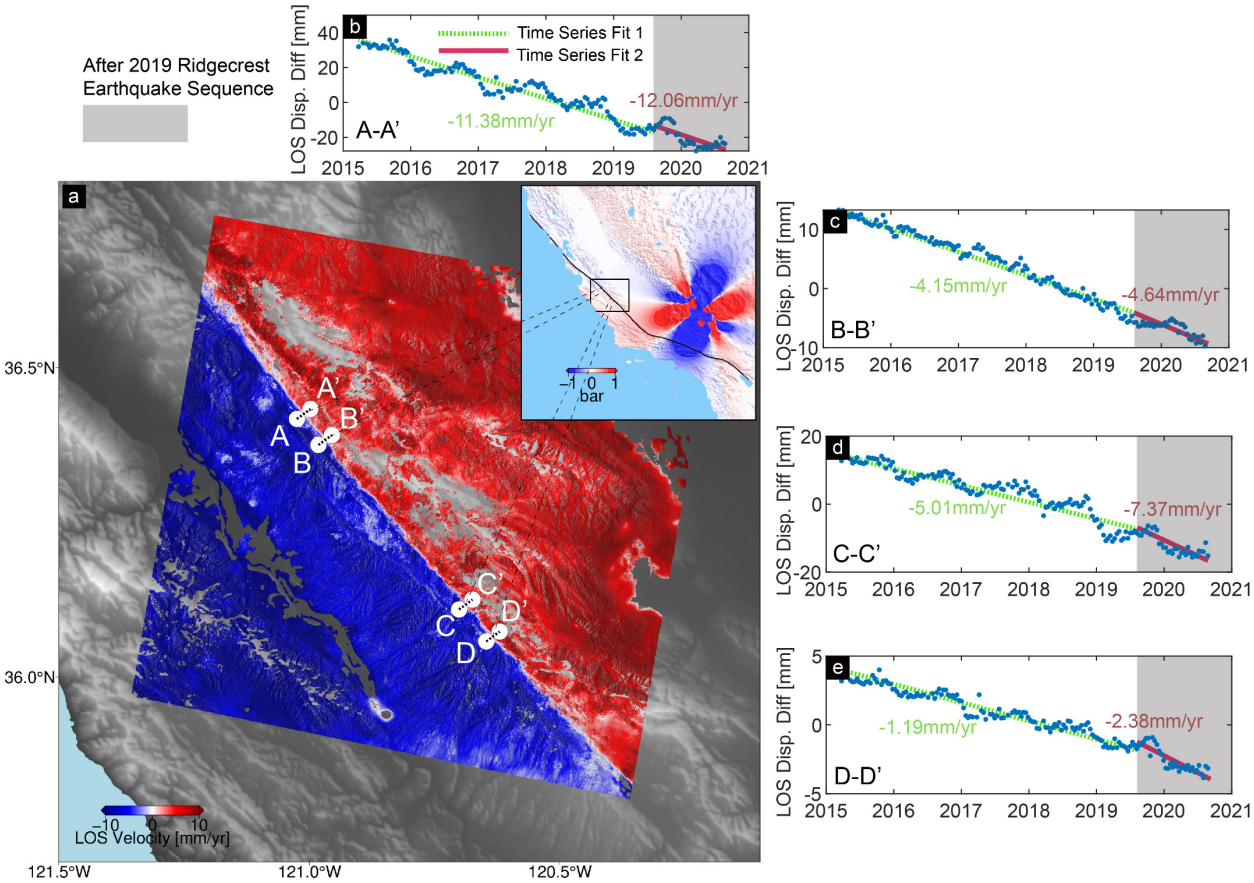

Figure 13. The static Coulomb stress change of 2019 Ridgecrest earthquake sequence and time series difference of eight points. (a) represents locations of the eight points. The subfigure in (a) is the calculated static Coulomb stress change. (b-e) are respectively time series difference of A-A', B-B', C-C' and D-D', respectively.

Except for the obvious rate changes, the time series also show the quasi-annual characteristics. Groundwater level due to seasonal rainfall (Roeloffs, 2001) and pumping-recharging (Chaussard *et al.*, 2014) can potentially explain the seasonal characteristics. We suggest that the combination of water table variations and local agriculture pumping is responsible for the oscillatory behavior. One can see that the peaks of the annual oscillation are all centered in the late autumn and winter instead of summer and spring. According to laboratory studies (Schulz *et al.*, 1983), a natural drop in water tables during the summer can make the slip zone deeper. The absence of groundwater will affect the stability and strain-hardening properties of fault clays (Morrow *et al.*, 1982). Thus, late autumn and winter, when continuous slip in depth eventually exceeds the surface strength

threshold, the accumulated shallow strain will be released in the event of continuous and large creep. In addition, the agricultural pumping can magnify this effect. It can also be an additional mechanism for the sometimes enlarged seasonal amplitude because additional stress may be concentrated in the shallow parts where compaction of local aquifers is associated with falling water tables.

5 Conclusions

We have developed an automatic phase unwrapping error correction approach for multi-looked InSAR data which combines decorrelation phase correction, phase triplet closure test and integer linear programming. We firstly tested our method on synthetic data, the results show that it can correct most of the unwrapping errors and benefit for InSAR LOS velocity estimation. Jackknife tests also demonstrate the improved uncertainty of creep model constrained by the LOS velocity after error correction. We also applied the proposed method to the Central San Andreas Fault. Experimental results validate the effectiveness of our proposed phase unwrapping error correction method, and it also suggest that the proposed is significant as a gain step for InSAR LOS velocity estimation and can further reduce the uncertainty of creep model.

Acknowledgments and Code Availability

This research was supported by the Fundamental Research Funds for the Central Universities (B210203079). We thank Wanpeng Feng in Sun Yat-Sen University for providing slip model of Ridgecrest Earthquake sequence. We deeply thank Mostafa for providing us the CASF model and his suggestions on the inversion. Good luck with your work in Deloitte. We acknowledge Plate Boundary Observatory, operated by UNAVCO for providing GPS data (https://www.unavco.org/data). We also thank USGS for providing recorded micro-seismicity (https://earthquake.usgs.gov/earthquakes). Sentinel-1 data were freely provided by the European Space Agency (https://scihub.copernicus.eu/). The GACOS atmospheric correction system for InSAR is available at http://www.gacos.net/#. Some figures were drawn by Generic Mapping Tools 6.1.0 software (https://www.generic-mapping-tools.org/download/, (Wessel *et al.*, 2019)). We provided a code copy supporting Sentinel-1 interferometric processing used in this paper online (https://zenodo.org/record/4774694).

References

Biggs, J., Wright, T., Lu, Z., and Parsons, B. (2007), Multi-interferogram method for measuring interseismic deformation: Denali Fault, Alaska, *Geophysical Journal International*, *170*(3), 1165-1179. doi: 10.1111/j.1365-246X.2007.03415.x.

Candes, E. J., and Tao, T. (2005), Decoding by linear programming, *IEEE Transactions on Information Theory*, *51*(12), 4203-4215. doi: 10.1109/TIT.2005.858979.

Chaussard, E., Bürgmann, R., Shirzaei, M., Fielding, E. J., and Baker, B. (2014), Predictability of hydraulic head changes and characterization of aquifer-system and fault properties from InSAR-derived ground deformation, *Journal of Geophysical Research: Solid Earth*, *119*(8), 6572-6590. doi: https://doi.org/10.1002/2014JB011266.

Chen, C. W., and Zebker, H. A. (2001), Two-dimensional phase unwrapping with use of statistical models for cost functions in nonlinear optimization, *J. Opt. Soc. Am. A*, *18*(2), 338-351. doi: 10.1364/JOSAA.18.000338.

Chen, S. S., Donoho, D. L., and Saunders, M. A. (2001), Atomic Decomposition by Basis Pursuit, *SIAM Review*, *43*(1), 129-159. doi: 10.1137/S003614450037906X.

Cigna, F., and Tapete, D. (2021), Satellite InSAR survey of structurally-controlled land subsidence due to groundwater exploitation in the Aguascalientes Valley, Mexico, *Remote Sensing of Environment*, *254*, 112254. doi: https://doi.org/10.1016/j.rse.2020.112254.

Costantini, M. (1998), A novel phase unwrapping method based on network programming, *IEEE Transactions on Geoscience and Remote Sensing*, *36*(3), 813-821. doi: 10.1109/36.673674.

Costantini, M., and Rosen, P. A. (1999), A generalized phase unwrapping approach for sparse data, paper presented at IEEE 1999 International Geoscience and Remote Sensing Symposium. IGARSS'99 (Cat. No. 99CH36293), IEEE.

Costantini, M., Malvarosa, F., and Minati, F. (2012), A General Formulation for Redundant Integration of Finite Differences and Phase Unwrapping on a Sparse Multidimensional Domain, *IEEE Transactions on Geoscience and Remote Sensing*, *50*(3), 758-768. doi: 10.1109/TGRS.2011.2162630.

De Zan, F., and Guarnieri, A. M. (2006), TOPSAR: Terrain observation by progressive scans, *IEEE Transactions on Geoscience and Remote Sensing*, *44*(9), 2352-2360.

Donoho, D. L. (2006), Compressed sensing, *IEEE Transactions on Information Theory*, *52*(4), 1289-1306. doi: 10.1109/TIT.2006.871582.

Donoho, D. L., and Elad, M. (2003), Optimally sparse representation in general (nonorthogonal) dictionaries via ℓ1 minimization, *Proceedings of the National Academy of Sciences*, *100*(5), 2197. doi: 10.1073/pnas.0437847100.

ElGharbawi, T., and Tamura, M. (2015), Coseismic and postseismic deformation estimation of the 2011 Tohoku earthquake in Kanto Region, Japan, using InSAR time series analysis and GPS, *Remote Sensing of Environment*, *168*, 374-387. doi: 10.1016/j.rse.2015.07.016.

Ester, M., Kriegel, H.-P., Sander, J., and Xu, X. (1996), A density-based algorithm for discovering clusters in large spatial databases with noise, paper presented at Kdd.

Fattahi, H. (2015), Geodetic imaging of tectonic deformation with InSAR, Ph.D. thesis, 190 pp, University of Miami, Ann Arbor.

Fattahi, H., Agram, P., and Simons, M. (2016), A network-based enhanced spectral diversity approach for TOPS time-series analysis, *IEEE Transactions on Geoscience and Remote Sensing*, *55*(2), 777-786.

Feng, G. C., Li, Z. W., Shan, X. J., Xu, B., and Du, Y. N. (2015), Source parameters of the 2014 Mw 6.1 South Napa earthquake estimated from the Sentinel 1A, COSMO-SkyMed and GPS data, *Tectonophysics*, *655*, 139-146. doi: 10.1016/j.tecto.2015.05.018.

Feng, W., Samsonov, S., Qiu, Q., Wang, Y., Zhang, P., Li, T., and Zheng, W. (2020), Orthogonal Fault Rupture and Rapid Postseismic Deformation Following 2019 Ridgecrest, California, Earthquake Sequence Revealed From Geodetic Observations, *Geophysical Research Letters*, *47*(5), e2019GL086888. doi: https://doi.org/10.1029/2019GL086888.

Ghiglia, D. C., and Romero, L. A. (1996), Minimum Lp-norm two-dimensional phase unwrapping, *J. Opt. Soc. Am. A*, *13*(10), 1999-2013. doi: 10.1364/JOSAA.13.001999.

Ghiglia, D. C., and Pritt, M. D. (1998), *Two-dimensional phase unwrapping: theory, algorithms, and software*, Wiley New York.

Hansen, P. C. (1994), REGULARIZATION TOOLS: A Matlab package for analysis and solution of discrete ill-posed problems, *Numerical Algorithms*, *6*(1), 1-35. doi: 10.1007/BF02149761.

Hanssen, R. F. (2001), *Radar interferometry: data interpretation and error analysis*, Springer Science & Business Media.

Hetland, E., and Hager, B. (2006), Interseismic strain accumulation: Spin‐up, cycle invariance, and irregular rupture sequences, *Geochemistry, Geophysics, Geosystems*, *7*(5).

Hooper, A., and Zebker, H. (2007), Phase unwrapping in three dimensions with application to InSAR time series, *J. Opt. Soc. Am. A*, *24*(9), 2737-2747.

Hooper, A., Zebker, H., Segall, P., and Kampes, B. (2004), A new method for measuring deformation on volcanoes and other natural terrains using InSAR persistent scatterers, *Geophysical research letters*, *31*(23).

Hussain, E., Hooper, A., Wright, T. J., Walters, R. J., and Bekaert, D. P. S. (2016), Interseismic strain accumulation across the central North Anatolian Fault from iteratively unwrapped InSAR measurements, *Journal of Geophysical Research: Solid Earth*, *121*(12), 9000-9019. doi: 10.1002/2016JB013108.

Itoh, K. (1982), Analysis of the phase unwrapping algorithm, *Applied Optics*, *21*(14), 2470-2470. doi: 10.1364/AO.21.002470.

Jong-Sen, L., Hoppel, K. W., Mango, S. A., and Miller, A. R. (1994), Intensity and phase statistics of multilook polarimetric and interferometric SAR imagery, *IEEE Transactions on Geoscience and Remote Sensing*, *32*(5), 1017-1028. doi: 10.1109/36.312890.

Khoshmanesh, M., and Shirzaei, M. (2018), Episodic creep events on the San Andreas Fault caused by pore pressure variations, *Nature Geoscience*, *11*(8), 610-614. doi: 10.1038/s41561-018-0160-2.

Khoshmanesh, M., and Shirzaei, M. (2018), Multiscale Dynamics of Aseismic Slip on Central San Andreas Fault, *Geophysical Research Letters*, *45*(5), 2274-2282. doi: https://doi.org/10.1002/2018GL077017.

Khoshmanesh, M., Shirzaei, M., and Nadeau, R. M. (2015), Time-dependent model of aseismic slip on the central San Andreas Fault from InSAR time series and repeating earthquakes, *Journal of Geophysical Research: Solid Earth*, *120*(9), 6658-6679. doi: 10.1002/2015JB012039.

Liu, F., and Pan, B. (2020), A New 3-D Minimum Cost Flow Phase Unwrapping Algorithm Based on Closure Phase, *IEEE Transactions on Geoscience and Remote Sensing*, *58*(3), 1857-1867. doi: 10.1109/TGRS.2019.2949926.

Ma, Z. F., Jiang, M., and Huang, T. (2020), A Sequential Approach for Sentinel-1 TOPS Time-Series Co-Registration Over Low Coherence Scenarios, *IEEE Transactions on Geoscience and Remote Sensing*, 1-9. doi: 10.1109/TGRS.2020.3009996.

Ma, Z. F., Jiang, M., Khoshmanesh, M., and Cheng, X. (2021), Time Series Phase Unwrapping Based on Graph Theory and Compressed Sensing, *IEEE Transactions on Geoscience and Remote Sensing*, 1-12. doi: 10.1109/TGRS.2021.3066784.

Michaelides, R. J., Zebker, H. A., and Zheng, Y. (2019), An Algorithm for Estimating and Correcting Decorrelation Phase From InSAR Data Using Closure Phase Triplets, *IEEE Transactions on Geoscience and Remote Sensing*, *57*(12), 10390-10397. doi: 10.1109/TGRS.2019.2934362.

Morrow, C. A., Shi, L. Q., and Byerlee, J. D. (1982), Strain hardening and strength of clay-rich fault gouges, *Journal of Geophysical Research: Solid Earth*, *87*(B8), 6771-6780. doi: https://doi.org/10.1029/JB087iB08p06771.

Okada, Y. (1992), Internal deformation due to shear and tensile faults in a half-space, *Bulletin of the Seismological Society of America*, *82*(2), 1018-1040.

Park, T., and Casella, G. (2008), The Bayesian Lasso, *Journal of the American Statistical Association*, *103*(482), 681-686. doi: 10.1198/016214508000000337.

Pepe, A., and Lanari, R. (2006), On the Extension of the Minimum Cost Flow Algorithm for Phase Unwrapping of Multitemporal Differential SAR Interferograms, *IEEE Transactions on Geoscience and Remote Sensing*, *44*(9), 2374-2383. doi: 10.1109/TGRS.2006.873207.

Perfettini, H., and Avouac, J. P. (2004), Postseismic relaxation driven by brittle creep: A possible mechanism to reconcile geodetic measurements and the decay rate of aftershocks, application to the Chi-Chi earthquake, Taiwan, *Journal of Geophysical Research: Solid Earth*, *109*(B2). doi: https://doi.org/10.1029/2003JB002488.

Roeloffs, E. A. (2001), Creep rate changes at Parkfield, California 1966–1999: Seasonal, precipitation induced, and tectonic, *Journal of Geophysical Research: Solid Earth*, *106*(B8), 16525-16547. doi: https://doi.org/10.1029/2001JB000352.

Rolandone, F., Bürgmann, R., Agnew, D. C., Johanson, I. A., Templeton, D. C., d'Alessio, M. A., Titus, S. J., DeMets, C., and Tikoff, B. (2008), Aseismic slip and fault-normal strain along the central creeping section of the San Andreas fault, *Geophysical Research Letters*, *35*(14). doi: https://doi.org/10.1029/2008GL034437.

Ryder, I., and Bürgmann, R. (2008), Spatial variations in slip deficit on the central San Andreas Fault from InSAR, *Geophysical Journal International*, *175*(3), 837-852. doi: 10.1111/j.1365-246X.2008.03938.x.

Schulz, S., Burford, R. O., and Mavko, B. (1983), Influence of seismicity and rainfall on episodic creep on the San Andreas Fault System in central California, *Journal of Geophysical Research: Solid Earth*, *88*(B9), 7475-7484. doi: https://doi.org/10.1029/JB088iB09p07475.

Scott, C., Bunds, M., Shirzaei, M., and Toke, N. (2020), Creep Along the Central San Andreas Fault From Surface Fractures, Topographic Differencing, and InSAR, *Journal of Geophysical Research: Solid Earth*, *125*(10), e2020JB019762. doi: https://doi.org/10.1029/2020JB019762.

Shanker, A. P., and Zebker, H. (2010), Edgelist phase unwrapping algorithm for time series InSAR analysis, *J. Opt. Soc. Am. A*, *27*(3), 605-612. doi: 10.1364/JOSAA.27.000605.

Shirzaei, M., Freymueller, J., Törnqvist, T. E., Galloway, D. L., Dura, T., and Minderhoud, P. S. J. (2021), Measuring, modelling and projecting coastal land subsidence, *Nature Reviews Earth & Environment*, *2*(1), 40-58. doi: 10.1038/s43017-020-00115-x.

Stramondo, S., Trasatti, E., Albano, M., Moro, M., Chini, M., Bignami, C., Polcari, M., and Saroli, M. (2016), Uncovering deformation processes from surface displacements, *Journal of Geodynamics*, *102*, 58-82. doi: 10.1016/j.jog.2016.08.001.

Walters, R. J., Holley, R. J., Parsons, B., and Wright, T. J. (2011), Interseismic strain accumulation across the North Anatolian Fault from Envisat InSAR measurements, *Geophysical Research Letters*, *38*(5). doi: https://doi.org/10.1029/2010GL046443.

Wang, H., Wright, T. J., Yu, Y., Lin, H., Jiang, L., Li, C., and Qiu, G. (2012), InSAR reveals coastal subsidence in the Pearl River Delta, China, *Geophysical Journal International*, *191*(3), 1119-1128. doi: 10.1111/j.1365-246X.2012.05687.x.

Wang, K., and Fialko, Y. (2018), Observations and Modeling of Coseismic and Postseismic Deformation Due To the 2015 Mw 7.8 Gorkha (Nepal) Earthquake, *Journal of Geophysical Research: Solid Earth*, *123*(1), 761-779. doi: https://doi.org/10.1002/2017JB014620.

Wang, K., and Burgmann, R. (2020), Co- and Early Postseismic Deformation Due to the 2019 Ridgecrest Earthquake Sequence Constrained by Sentinel-1 and COSMO-SkyMed SAR Data, *Seismological Research Letters*, *91*(4), 1998-2009. doi: 10.1785/0220190299.

Wessel, P., Luis, J. F., Uieda, L., Scharroo, R., Wobbe, F., Smith, W. H. F., and Tian, D. (2019), The Generic Mapping Tools Version 6, *Geochemistry, Geophysics, Geosystems*, *20*(11), 5556-5564. doi: https://doi.org/10.1029/2019GC008515.

Wright, T., Parsons, B., and Fielding, E. (2001), Measurement of interseismic strain accumulation across the North Anatolian Fault by satellite radar interferometry, *Geophysical Research Letters*, *28*(10), 2117-2120. doi: https://doi.org/10.1029/2000GL012850.

Xu, W., Wu, S., Materna, K., Nadeau, R., Floyd, M., Funning, G., Chaussard, E., Johnson, C. W., Murray, J. R., Ding, X., and Bürgmann, R. (2018), Interseismic Ground Deformation and Fault Slip Rates in the Greater San Francisco Bay Area From Two Decades of Space Geodetic Data, *Journal of Geophysical Research: Solid Earth*, *123*(9), 8095-8109. doi: https://doi.org/10.1029/2018JB016004.

Xu, X., and Sandwell, D. T. (2020), Toward Absolute Phase Change Recovery With InSAR: Correcting for Earth Tides and Phase Unwrapping Ambiguities, *IEEE Transactions on Geoscience and Remote Sensing*, *58*(1), 726-733. doi: 10.1109/TGRS.2019.2940207.

Xu, X., Ward, L. A., Jiang, J., Smith-Konter, B., Tymofyeyeva, E., Lindsey, E. O., Sylvester, A. G., and Sandwell, D. T. (2018), Surface Creep Rate of the Southern San Andreas Fault Modulated by Stress Perturbations From Nearby Large Events, *Geophysical Research Letters*, *45*(19), 10,259-210,268. doi: https://doi.org/10.1029/2018GL080137.

Yu, C., Li, Z., Penna, N. T., and Crippa, P. (2018), Generic Atmospheric Correction Model for Interferometric Synthetic Aperture Radar Observations, *Journal of Geophysical Research: Solid Earth*, *123*(10), 9202-9222. doi: https://doi.org/10.1029/2017JB015305.

Yu, H., Lan, Y., Xu, J., An, D., and Lee, H. (2017), Large-Scale L0 -Norm and L1 -Norm 2-D Phase Unwrapping, *IEEE Transactions on Geoscience and Remote Sensing*, *55*(8), 4712-4728. doi: 10.1109/TGRS.2017.2698452.

Zan, F. D., Zonno, M., and López-Dekker, P. (2015), Phase Inconsistencies and Multiple Scattering in SAR Interferometry, *IEEE Transactions on Geoscience and Remote Sensing*, *53*(12), 6608-6616. doi: 10.1109/TGRS.2015.2444431.

Zheng, Y., Zebker, H., and Michaelides, R. (2021), A New Decorrelation Phase Covariance Model for Noise Reduction in Unwrapped Interferometric Phase Stacks, *IEEE Transactions on Geoscience and Remote Sensing*, 1-10. doi: 10.1109/TGRS.2021.3050087.